ARTICLE

Evaluating the Efficiency of Boron Nitride Coating in Single-Walled Carbon-Nanotube-Based 1D Heterostructure Films by Optical Spectroscopy

Shuhui Wang,[⊥] Dmitry I. Levshov,*,[⊥] Keigo Otsuka, Bo-Wen Zhang, Yongjia Zheng, Ya Feng, Ming Liu, Esko I. Kauppinen, Rong Xiang, Shohei Chiashi, Wim Wenseleers, Sofie Cambré, and Shigeo Maruyama*

Read Online

ACCESS | Metrics & More | Article Recommendations | SI Supporting Information

ABSTRACT: Single-walled carbon nanotube (SWCNT) films exhibit exceptional optical and electrical properties, making them highly promising for scalable integrated devices. Previously, we employed SWCNT films as templates for the chemical vapor deposition (CVD) synthesis of one-dimensional heterostructure films where boron nitride nanotubes (BNNTs) and molybdenum disulfide nanotubes (MoS$_2$NTs) were coaxially nested over the SWCNT networks. In this work, we have further refined the synthesis method to achieve precise control over the BNNT coating in SWCNT@BNNT heterostructure films. The resulting structure of the SWCNT@BNNT films was thoroughly characterized using a combination of electron microscopy, UV−vis−NIR spectroscopy, Fourier-transform infrared (FT-IR) spectroscopy, and Raman spectroscopy. Specifically, we investigated the pressure effect induced by BNNT wrapping on the SWCNTs in the SWCNT@BNNT heterostructure film and demonstrated that the shifts of the SWCNT's G and 2D (G′) modes in Raman spectra can be used as a probe of the efficiency of BNNT coating. In addition, we studied the impact of vacuum annealing on the removal of the initial doping in SWCNTs, arising from exposure to ambient atmosphere, and examined the effect of MoO$_3$ doping in SWCNT films by using UV−vis−NIR spectroscopy and Raman spectroscopy. We show that through correlation analysis of the G and 2D (G′) modes in Raman spectra, it is possible to discern distinct types of doping effects as well as the influence of applied pressure on the SWCNTs within SWCNT@BNNT heterostructure films. This work contributes to a deeper understanding of the strain and doping effect in both SWCNTs and SWCNT@BNNTs, thereby providing valuable insights for future applications of carbon-nanotube-based one-dimensional heterostructures.

KEYWORDS: one-dimensional heterostructure, single-walled carbon nanotube, boron nitride nanotube, Raman spectroscopy, van der Waals
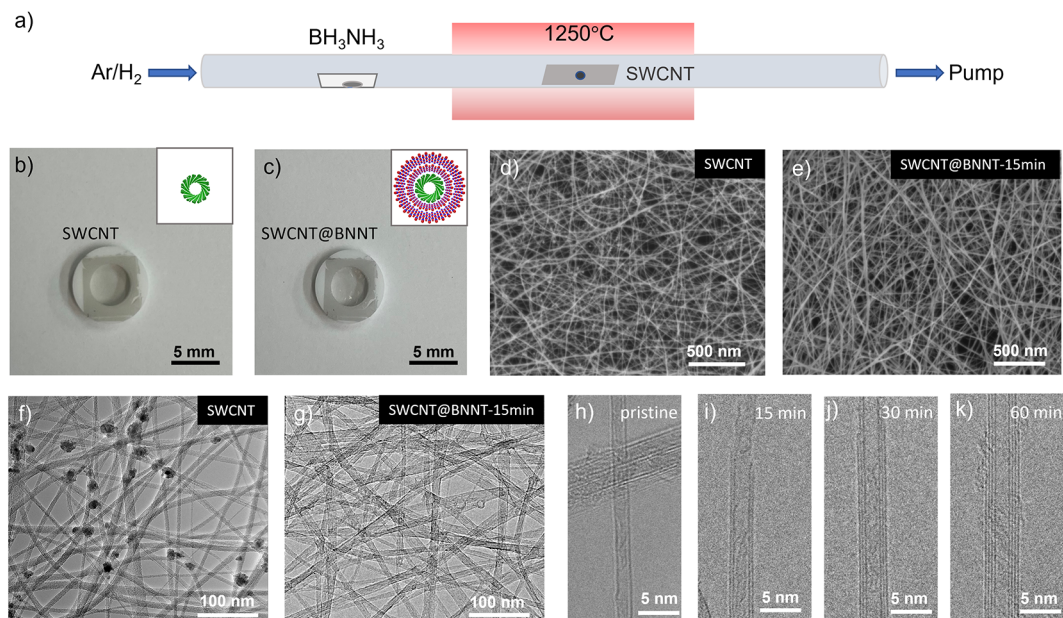
SWCNT@BNNT film
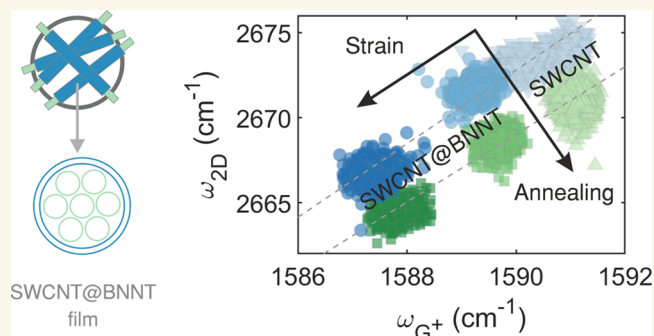
INTRODUCTION

One-dimensional van der Waals (1D vdW) heterostructures are an emerging class of nanomaterials that consist of coaxially stacked atomically thin layers, including graphene, boron nitride (BN), molybdenum disulfide (MoS$_2$), tungsten disulfide (WS$_2$), and others.[1,2] Each of these layers exhibits distinct physical properties, with some being metallic, semiconducting, or insulating.[3] Combining them into a single structure not only leads to a vast number of potential applications in various fields, including (opto)electronics, photovoltaics, and electrochemis-

A

Figure 1. Fabrication of SWCNT@BNNT heterostructure films. (a) Schematic illustration of the CVD process for growing the SWCNT@BNNT heterostructure film. Photographs of (b) an SWCNT film suspended on a ceramic washer and (c) an SWCNT@BNNT film after BNNT wrapping, demonstrating the macroscopic morphology of the film samples. Insets show the corresponding atomic models of the SWCNT and SWCNT@BNNT. SEM images of (d) a pristine SWCNT film and (e) an SWCNT@BNNT film after 15 min of CVD growth. TEM images of (f) a pristine SWCNT film and (g) a SWCNT@BNNT film after 15 min of CVD growth. TEM images of a representative individual tube in (h) a pristine SWCNT film and SWCNT films after different BN CVD growth times: (i) 15 min; (j) 30 min; (k) 60 min (for figures corresponding to longer growth times, refer to Figure S1 in Section S1 in the Supporting Information (SI)).

try,[4,5] but also results in intriguing physical phenomena arising from crystal lattice mismatch or quantum confinement, such as moiré flat bands and strongly correlated electronic states.[6,7]

Among the promising types of 1D vdW heterostructures are single-walled carbon nanotubes (SWCNTs) encapsulated in BN tubes (SWCNT@BNNTs). They have been suggested as candidates for back-gate field-effect transistors,[1] the smallest coaxial cables,[8] model topological insulators for low-power electronics,[9] or templates for the growth of much larger 1D heterostructures such as BNNT@MoS$_2$.[1,10,11] Although recently significant progress has been made in the synthesis of SWCNT@BNNTs by utilizing chirality-sorted SWCNTs,[12,13] further advancements in their controlled growth, in particular for macroscopic quantities, require fast and reliable characterization tools that provide information on the synthesis efficiency and material structure and quality.[6,7]

Optical spectroscopy is a highly effective technique for characterizing 1D vdW structures, as their electronic, optical, and vibrational properties are modulated by the vdW mechanical and electronic couplings being a function of the diameter, interlayer distance, interlayer twist angle, strain, interlayer charge, and energy transfer.[7] This can be illustrated by the simplest and yet best-studied 1D vdW structures, which are double-walled carbon nanotubes (DWCNTs).[7] Raman spectroscopy, for example, can accurately estimate the diameters and interlayer distances of DWCNTs by analyzing the radial breathing modes (RBM)[14,15] and G modes[16] or probe the metallicity of the layers based on the G line shape[17] or electronic Raman scattering peaks.[18] The exact inner@outer tube combinations of DWCNTs can be identified by inspecting the RBM frequencies and transition energies in the Raman excitation profiles influenced by moiré-induced vibrational coupling[19,20] or based on the optical features originating from the intertube transitions in the Rayleigh spectra,[21,22] optical

absorption spectra and Raman excitation profiles.[23] Alternatively, they can be deduced from inspecting the intertube energy transfer peaks as was shown recently by Erkens et al. combining absorption spectroscopy, photoluminescence excitation spectroscopy (PLE), and tunable Raman spectroscopy.[19] Optical spectroscopy has been also successfully employed for investigating more complex 1D vdW structures such as SWCNT@BNNTs based on different SWCNT templates, e.g. vertically aligned SWCNT@BNNT heterostructure layers,[24] and zeolite-supported SWCNT@BNNT heterostructures.[25]

In this work, we employed a range of optical spectroscopy techniques, including UV−vis−NIR spectroscopy, Fourier-transform infrared (FT-IR) spectroscopy, and Raman spectroscopy, to thoroughly characterize and analyze the optical properties of the SWCNT@BNNT heterostructure films. In particular, we investigated the pressure effect resulting from BNNT wrapping on the SWCNTs within the SWCNT@BNNT heterostructure film, demonstrating that the shifts observed in the G and 2D (G') modes of SWCNTs can serve as a probe of the efficiency of BNNT coating. Additionally, we studied the impact of vacuum annealing on the removal of the initial doping in SWCNTs, arising from exposure to the ambient atmosphere, and examined the effect of MoO$_3$ doping in SWCNT films, using UV−vis−NIR spectroscopy and Raman spectroscopy. We demonstrate that by performing the correlation analysis of the G and 2D (G') modes in Raman spectra, it is possible to distinguish distinct types of doping effects as well as the influence of applied pressure on the SWCNTs within SWCNT@BNNT heterostructure films.

RESULTS AND DISCUSSION

Synthesis and Structure Analysis of SWCNT@BNNT Heterostructure Films. In our previous studies, we estab-
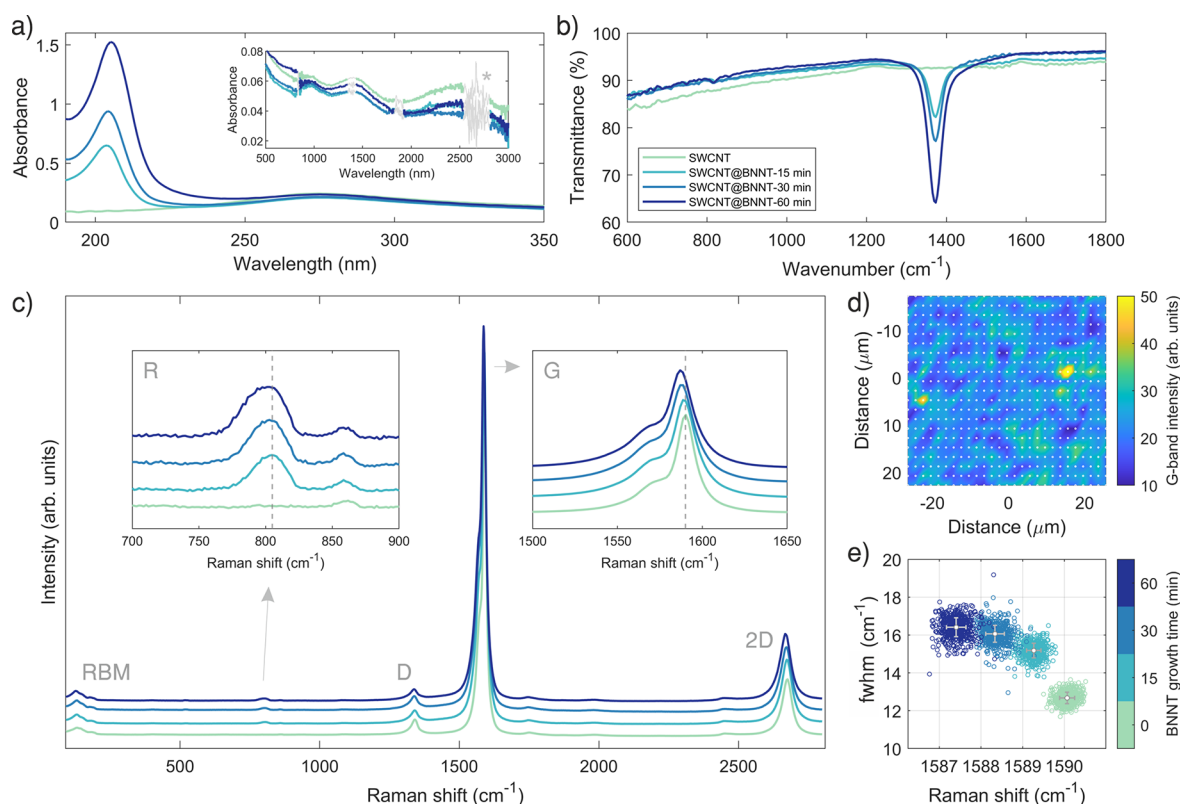
Figure 2. Optical characterization of SWCNT and SWCNT@BNNT heterostructure films. (a) Optical absorption spectra of SWCNT and SWCNT@BNNT heterostructure films. The inset shows the zoomed-in optical absorption spectra in the range from 500 to 3000 nm of the same samples. The gray region marked by a star is caused by a strong absorption from the ambient atmosphere, preventing this region from being measured accurately. (b) FT-IR spectra of the pristine SWCNT film and SWCNT@BNNT heterostructure films. (c) Average Raman spectra over an area of approximately $52\,\mu m \times 40\,\mu m$ of the pristine SWCNT and SWCNT@BNNT heterostructure films with an excitation wavelength of 532 nm. Inserted figures are the enlarged Raman spectra focusing on the region around 800 cm^{-1} (left) and the G-band region (right) of the SWCNT and SWCNT@BNNT heterostructure films. (d) Raman intensity map of the scanning area of SWCNT@BNNT heterostructure film with a CVD growth time of 15 min. (e) Scatter plot of fwhm of G$^+$ peak against its position for SWCNT films with different BN CVD growth times.

lished a method for growing coaxial SWCNT@BNNT heterostructures by a CVD technique.[1,12] In this work, we extended this method further, primarily by optimizing the CVD growth temperature, allowing for even greater control over the BNNT coating in the SWCNT@BNNT heterostructure films. The approach and results of this development are illustrated in Figure 1. To grow heterostructures, we used an SWCNT film as a template and ammonia−borane as the precursor (Figure 1a). To avoid any effect from the substrate during subsequent spectroscopic characterizations, we suspended both pristine SWCNT film and SWCNT@BNNT films on ceramic washers with a 4 mm inner diameter, as shown in the photographs in Figure 1b,c, respectively.

Our findings demonstrate that the quality of BNNT crystallization can be effectively controlled by the high-temperature treatment (1250 °C). For instance, we refer to the scanning electron microscopy (SEM) and transmission electron microscopy (TEM) images in Figure 1d,f, which illustrate the morphology of the pristine SWCNT film before the BN CVD process. Particularly, small dark spots are observed in both images, which correspond to the catalyst particles remaining after the fabrication of SWCNT networks.[26,27] These catalyst particles are removed by high-temperature treatment during the CVD process, as evidenced by the SEM and TEM images of the SWCNT@BNNT film for 15 min of

CVD growth time (denoted as SWCNT@BNNT-15; see Figure 1e,g, respectively).

Moreover, with an increase in the BN growth time, the thickness of the SWCNT@BNNT networks increases, indicating successful wrapping of BN layers around the SWCNT template. SEM and TEM images of SWCNT@BNNT for a 30 min CVD growth time (SWCNT@BNNT-30) are shown in Figure S1a,c, respectively, while those for 60 min of growth (SWCNT@BNNT-60) are presented in Figure S1b,d. The latter images reveal the thickest BN layers among the three different growth conditions. It is worth noting that no two-dimensional h-BN flakes are observed under those BN CVD conditions even when the growth time is 60 min.

To better illustrate the change in the number of BN layers, we present typical individual carbon nanotubes in the pristine SWCNT film and SWCNT@BNNT films after three different BN CVD growth times (15, 30, and 60 min) in Figure 1h−k. It is clear that during the BN CVD process, highly crystalline BN layers are formed along the SWCNT. The number of BN layers is expected to increase with growth time; e.g. when the BN CVD growth time is 60 min, the number of BN layers reaches 2−3 layers, fully wrapping the individual carbon nanotube.

Spectroscopic Characterization of SWCNT and SWCNT@BNNT Heterostructure Films. By characterizing the aforementioned heterostructure films with various optical spectroscopic techniques, we have identified several character-
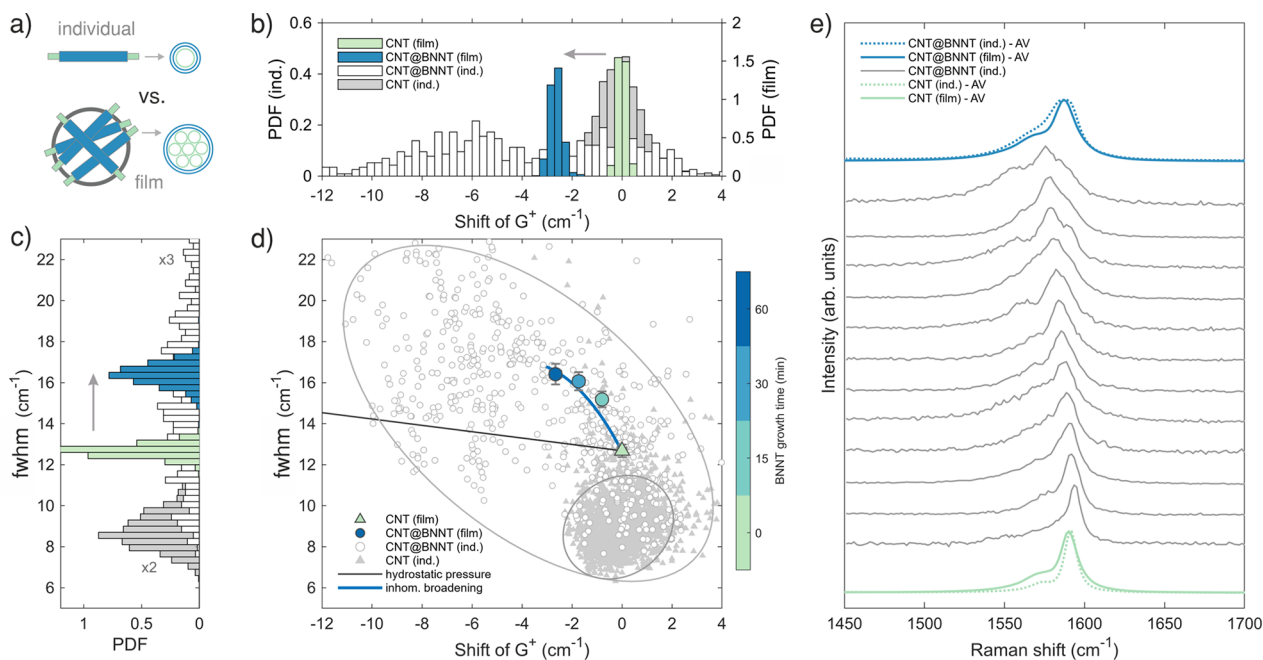
Figure 3. G-band behavior in individual and film SWCNT@BNNT samples. (a) Schematic representation of individual and film samples of SWCNT@BNNTs. **(b)** Frequency shift distribution of individual SWCNT@BNNTs (white histogram) displaying distinct peaks at 0 and −6.3 cm^{-1}, contrasting with the one-peak frequency shift distribution in the film sample (blue histogram). Dark gray and light green histograms represent individual and pristine SWCNT film samples, respectively. The arrow indicates the frequency shift of the G band upon BNNT growth. **(c)** fwhm distribution of individual SWCNT (dark gray), individual SWCNT@BNNTs (white), film SWCNT (light green), and film SWCNT@ BNNT (blue) samples. **(d)** Scatter plot illustrating the variation in frequency and fwhm of the most intense G$^+$ peak in the G band for individual SWCNT (filled triangles), individual SWCNT@BNNT (open circles), SWCNT film (light green triangle), and SWCNT@BNNT film (blue points) samples. The color of the film SWCNT@BNNT points represents the BNNT growth time. The solid blue and black lines represent the effects of inhomogeneous broadening and pressure, respectively. Small and large ellipses depict the range of frequency and fwhm variation for individual SWCNT and SWCNT@BNNT samples, respectively. **(e)** Raman spectra of selected individual SWCNT@BNNTs along the major axis of the ellipse in (d), demonstrating a gradual frequency shift and broadening (gray lines). The dashed green and blue lines correspond to averaged spectra from individual SWCNTs and SWCNT@BNNTs, respectively, resembling the spectra from the SWCNT and SWCNT@ BNNT film samples (solid green and blue lines).

istic signatures of the BN coating, as summarized in Figure 2. For instance, we observe a peak at ∼205 nm in the optical absorption spectra of SWCNT@BNNT films (Figure 2a) whose intensity grows with the increase in BN CVD growth time (represented by a color gradient in Figure 2; see legend). This peak is absent in the pristine SWCNT film; hence, we attribute it to the band gap optical transition of the BNNTs.[28] Moreover, the S$_{11}$ and S$_{22}$ peaks of the inner SWCNTs at 2600 and 1400 nm, respectively, exhibit intensity variation upon thermal annealing (inset of Figure 2a), which will be discussed in more detail later.

Another distinctive optical signature is an intense band at ∼1370 cm^{-1}, which can be observed in the FT-IR spectra of the SWCNT@BNNT films (Figure 2b). This particular peak is attributed to the longitudinal optical mode with vibrations along the axis of a BNNT,[29] equivalent to the in-plane stretching E$_{2g}$ mode of the h-BN. Similarly to optical absorption, the intensity of this FT-IR peak demonstrates a clear correlation with the increase in BN coating amount during CVD growth, as evident in Figure 2b.

Furthermore, we observe several significant changes in the Raman spectra of heterostructure films upon the BN coating. These changes are best illustrated using the Raman spectra of SWCNT and SWCNT@BNNT films in Figure 2c, which are obtained by averaging the data from the Raman maps measured with a 532 nm excitation. Specifically, we detect the appearance of a weak peak at ∼800 cm^{-1} (left inset in Figure 2c), which we attribute to the out-of-plane radial buckling mode of

BNNTs,[29,30] and a downshift of the Raman-active modes of SWCNTs such as RBM, G, and 2D bands (see the right inset in Figure 2c, zooming in on the G-band as an example). Interestingly, as in previous studies on vertically aligned SWCNT@BNNTs,[24] the A$_1$ Raman line of BNNTs located around 1370 cm^{-1} is not initially observed and becomes prominent only after burning the inner SWCNTs.[24] We note that the frequency shifts of the CNT and BNNT peaks in the Raman spectra correlate well with the increase of the number of BN layers during CVD growth, as observed in the SEM and TEM images (Figure 1). Consequently, these shifts can be readily used for estimating the efficiency of the BN coating during the CVD process. In the following, we will focus on the most intense among them, namely the G and 2D bands of SWCNTs, because of their higher signal-to-noise ratio.

To provide a more reliable evaluation of the efficiency of the BN coating in macroscopic film samples, we developed a characterization approach based on Raman imaging. In particular, we scan an area of approximately 52 μm × 40 μm with a step size of 2 μm, collecting over 500−600 spectra for each sample (see Figure 2d showing the intensity of the G band at the SWCNT film's surface). Each spectrum of the map is then fitted with a set of Lorentzian functions to obtain information on the positions, full widths at half-maximum (fwhm), and peak intensities of the main Raman lines (see details in SI Section S2). We reveal small variations in all of these parameters across the surface of the film samples, resulting in the formation of clusters

or clouds, as shown in the fwhm vs G^+ frequency plots (Figure 2e, where each circle represents a single measurement). Within each cluster, the standard deviations from the mean values of the G^+ mode frequency and fwhm constitute on average 0.2 and 0.3 cm^{-1}, respectively. This implies that the absolute difference between the minimum and maximum values of the frequency and fwhm within a cloud can reach 1 and 1.5 cm^{-1}, respectively. Such differences are of the same order of magnitude as the mean G shift at different CVD growth times, as is evident when comparing the centers of the clusters in Figure 2e. Consequently, using single-point measurements becomes unreliable for characterizing the film samples, as the obtained G band shift can vary significantly depending on which data point within the data cloud is measured. To address this issue, we compared samples using the mean values and standard deviations (reported as error bars) of the fitted fwhm and G^+ mode frequencies rather than reporting values for individual data points. For example, the effect of BN coating on the SWCNTs' Raman lines obtained from Raman imaging is illustrated in Figure 2e. After 15 min of BN CVD growth, the mean position of the G^+ mode shifted from 1590.1 cm^{-1} for the pristine SWCNT film to 1589.3 cm^{-1}. With increasing BN growth time, the downshift becomes more significant, ranging from 1588.3 cm^{-1} (SWCNT@BNNT-30) to 1587.4 cm^{-1} (SWCNT@BNNT-60). We also observed a broadening of the G^+ mode of SWCNTs after BNNT wrapping, as evidenced by the change in its mean fwhm from 12.7 cm^{-1} for a pristine SWCNT to 16.4 cm^{-1} (SWCNT@BNNT-60).

To gain further insights into the G-band behavior in film samples, we compare our experimental data with the Raman imaging data obtained by Matsushita et al.[5] on individual SWCNT and SWCNT@BNNTs on substrates (Figure 3a). The BNNTs in film and individual heterostructures were grown by using the same CVD method and should provide information on the intrinsic G-band behavior in single heteronanotubes. The differences between the two types of samples are best illustrated using the frequency and fwhm distributions (Figure 3b,c) or scatter plots (Figure 3d), where the histograms in Figure 3b,c are directly related to the data clusters in Figure 3d. For brevity, we present the data only from two film samples: the reference SWCNT and SWCNT@BNNT-60 samples (light green and dark blue histograms, respectively). We remark that due to the different mean G band frequencies in individual and film SWCNT templates, originating from diverse synthesis methods (alcohol-assisted CVD for individual SWCNTs versus aerosol CVD for SWCNT films), we compare in Figures 3b,d not the absolute G^+ frequencies, but the shift between the G^+ values in SWCNT@BNNTs and SWCNT template samples. The mean G^+ frequency of the pristine SWCNT sample is taken as the zero point.

Importantly, the frequency distribution of individual SWCNT@BNNTs reveals two distinct peaks at 0 and −6.3 cm^{-1}, represented by the maxima in the white histogram in Figure 3b (see also SI Section S3). These peaks are associated with large standard deviations of 1.9 and 3.4 cm^{-1}, respectively. In consequence, the absolute frequency shift within the distribution varies from +4 to −13 cm^{-1}, as visually highlighted by the large ellipse in Figure 3d. It contrasts with the one-peak frequency distribution from the film samples, with a much narrower standard deviation of 0.2 cm^{-1} (refer to the blue histogram in Figure 3b or error bars of the film points in Figure 3d).

We recall that the G-band shift of the inner SWCNTs was previously observed in individual DWCNTs[16] and MWCNTs[31] and in individual SWCNT@BNNTs[5] and explained in terms of an expansion of the inner SWCNTs due to the interlayer mechanical coupling. In particular, Popov et al.[16] calculated the dependence of the G-shift on the diameter and interlayer distance in DWCNTs. Furthermore, Matsushita et al.[5] developed a model accounting for the mechanical interaction in multilayered heterostructures and predicted the dependence of the G shift on the diameter of SWCNT@BNNTs. Based on these works, we can assign the first peak at 0 cm^{-1} in the individual SWCNT@BNNT distribution to either the presence of uncoated sections of SWCNTs in the sample after the BN CVD growth or contributions from the SWCNT@BNNT heterostructures with minimal interlayer mechanical coupling and hence negligible G band shift. The second peak at −6.3 cm^{-1} is due to the large abundance of SWCNT@BNNT heterostructures with a well-defined average diameter, interlayer distance, and number of BN layers.

Regarding the comparison of line widths, the average fwhm of G^+ peaks in individual SWCNTs is relatively small, measuring 7.7 cm^{-1}, compared to the film SWCNT sample with a value of 12.8 cm^{-1} (indicated by the gray and light green histograms in Figure 3c, respectively). However, the standard deviation of the fwhm for the individual SWCNTs is considerably larger, measuring 1.7 cm^{-1}, in contrast to the film samples with a value of 0.5 cm^{-1}.

To explain the observed differences between individual and film samples, it is important to consider that the film data result from averaging Raman responses of many SWCNTs and SWCNT@BNNTs under a laser beam. Therefore, they are influenced by the inhomogeneous broadening effect. To illustrate this, we plot the Raman spectra of various individual SWCNT@BNNTs from Matsushita et al.[5] (gray lines in Figure 3e) corresponding to the data points located along the major axis of the large ellipse in Figure 3d. Specifically, the data points from the bottom-right to the top-left corners of the ellipse are plotted from bottom to top, respectively. It is evident that the G bands in these selected Raman spectra exhibit a gradual frequency shift and broadening. These shifts are expected to correlate with the SWCNT@BNNT structure, including the average diameter, interlayer distance, and number of layers, as discussed earlier. Conversely, the broadening can be attributed to the uneven BN coating along the heterostructures, as reported in ref 5. Indeed, certain spectra display a three-peak structure, where the high-frequency peak likely corresponds to the signal from uncoated SWCNTs, which persist at specific points within the heterostructures.

Notably, by averaging all Raman spectra from individual SWCNTs and individual SWCNT@BNNTs, we obtain the spectra shown in Figure 3e with the dashed green and blue lines, respectively. They closely resemble the spectra from the SWCNT and SWCNT@BNNT film samples, averaged over all points on the film surface (solid green and blue lines in Figure 3e). Interestingly, the frequency difference between G^+ peaks in averaged individual SWCNT and SWCNT@BNNT spectra is about −3.3 cm^{-1}, which is quite close to the largest downshift of the G-band in film samples, i.e. the one in the SWCNT@BNNT-60 sample ($=$−2.7 cm^{-1}). The inhomogeneous broadening also accounts for the difference between the G band line widths in the individual SWCNT and film SWCNT samples (dark gray versus light green histograms in Figure 3c with centers at 7.7 and 12.8 cm^{-1}, respectively), as upon averaging,
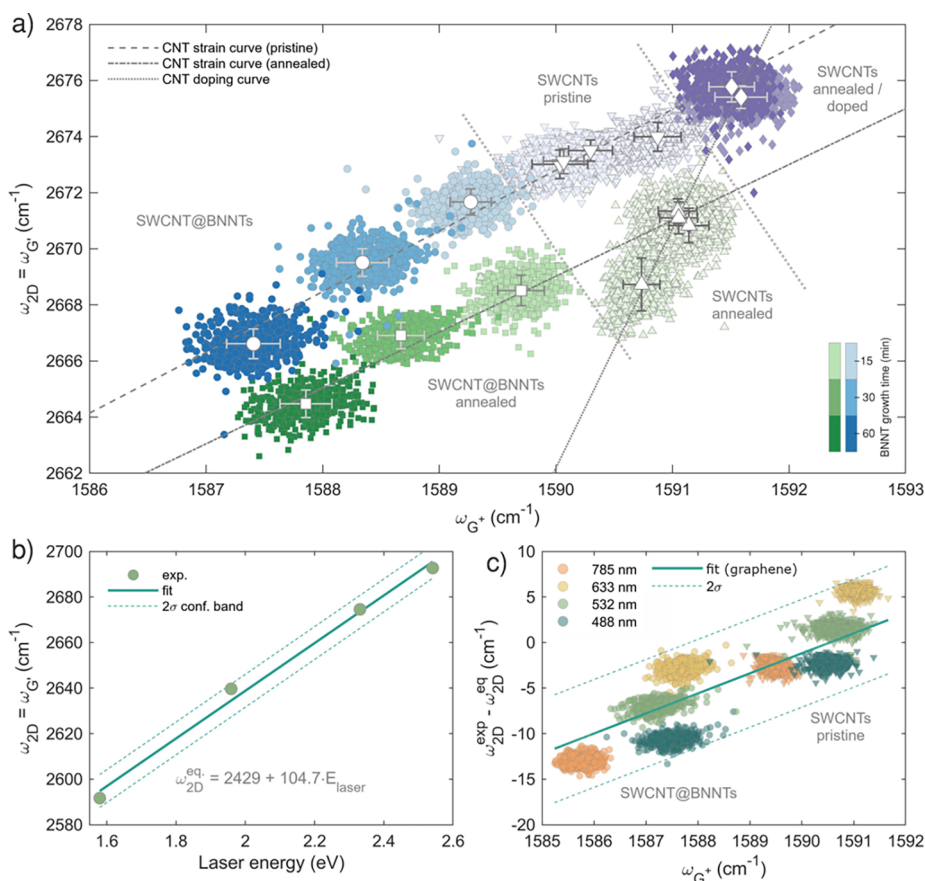
Figure 4. (a) Correlation between the frequencies of the G$^+$ and 2D (G') Raman modes of SWCNTs obtained from Raman mapping of different samples measured at 532 nm. The samples are categorized into five groups: pristine SWCNTs (light purple), SWCNT@BNNTs (blue), annealed SWCNTs (light green), annealed SWCNT@BNNTs (green), and annealed/doped SWCNTs (purple). Different shades of blue and green represent the growth times (see color bars). The annealed/doped SWCNT group consists of annealed SWCNT films doped with a MoO$_3$ layer with thicknesses of 1 nm (medium purple) and 4 nm (dark purple), respectively. The gray dashed, dash-dotted, and dotted lines correspond to the strain curve for the pristine SWCNT@BNNT samples, strain curve for the annealed SWCNT@BNNT samples, and the doping curve for the annealed/doped SWCNT samples, respectively. These curves were obtained by fitting the corresponding data clusters and are similar to the graphene strain and doping lines from the work of Lee et al.[33] (b) Frequency of the 2D (G') Raman mode as a function of excitation laser energy for pristine SWCNT films. The green solid line refers to the fit of the experimental data. The two green dashed lines indicate the 2σ confidence band. (c) Correlation between the frequencies of the G$^+$ peak and $\omega_{2D}^{exp} - \omega_{2D}^{eq}$ of SWCNT film sample and SWCNT@ BNNT film sample measured under four different excitation wavelengths (488, 532, 633, and 785 nm). Inverted triangle symbols denote the pristine SWCNT film samples, while circles correspond to the SWCNT@BNNT-60 sample. The green solid line represents the graphene strain curve with the slope 2.2.[33] The green dashed lines denote the 2σ confidence interval.

the fwhm of the former spectra increases to 14.5 cm^{-1}, which is rather close to the film samples.

Based on the observations provided, we propose the following mechanism to explain the frequency shift and line broadening of the G band in film samples. Each individual SWCNT in the SWCNT@BNNT films experiences varying levels of interlayer mechanical coupling, determined by factors such as the diameter, interlayer distance, and number of BN layers, which are all influenced by the growth conditions. This variation leads to frequency and fwhm distributions similar to those observed in the individual SWCNT@BNNT samples in Figure 3b,c (white histograms). Averaging the Raman responses of the entire ensemble of SWCNT@BNNTs under the laser beam results in both shifted and broadened G-band spectra compared with the SWCNT template case.

The gradual increase in both the frequency and fwhm in film samples, from SWCNT@BNNT-15 to SWCNT@BNNT-60, may be attributed to the gradual increase in the mechanical-coupling-induced peak at −6.3 cm^{-1} in the SWCNT@BNNT

frequency distribution with increasing BN growth time. This effect is depicted by the solid blue line in Figure 3d (see also SI Section S4).

Furthermore, it is of particular interest to compare the inhomogeneous broadening resulting from averaging over a wide distribution of SWCNT@BNNTs with the intrinsic broadening of the G band caused by the hydrostatic pressure.[32] In Figure 3d, the solid black line represents the latter effect extrapolated to negative pressure (SI Section S5), where the change in the fwhm with the G$^+$ shift is noticeably smaller than the measured broadening of the G band in the film samples, as indicated by the filled circles. Therefore, while the intrinsic broadening alone cannot fully explain the observed behavior, it may contribute to a lesser extent.

Finally, it is important to address whether the structural parameters of SWCNTs and BNNTs can be extracted from the observed G band shift in the SWCNT@BNNT films. For example, Figure 1i−k suggests that the number of BN layers in the heterostructures increases with the growth time, along with
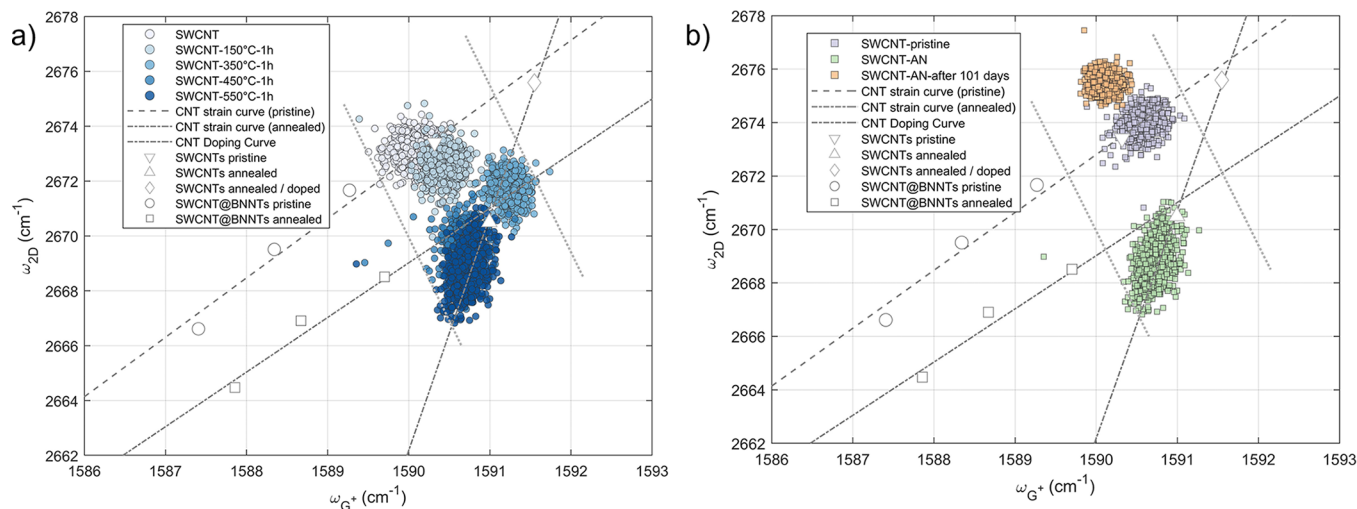
Figure 5. (a) Correlation between the frequency of the G$^+$ and 2D (G$'$) Raman mode of the SWCNT films treated under different conditions; (b) Evolution of Raman (ω_{G^+}, ω_{2D}) correlation map of air decay behavior from SWCNT film. The marks and dotted lines come from Figure 4a.

the absolute value of the G$^+$ shift (Figure 2e). However, establishing a direct correlation between these parameters is challenging because the G band shift is not only dependent on the number of layers; it also relies on the average diameter and interlayer distance, as predicted by Matsushita et al.[5] In consequence, further experimental work on structure-identified SWCNT@BNNTs is necessary to unambiguously determine such dependences, which goes beyond the scope of the current article.

Correlation between G$^+$ and 2D (G$'$) Band Frequencies. In the previous section, we attributed the downshift of the G$^+$ mode frequency in the SWCNT@BNNT heterostructures to the pressure effect caused by the mechanical interaction between the inner SWCNT and outer BNNT layers. However, since both pressure (strain) and doping can cause G band shifting, it is crucial to find an effective way to distinguish between these two factors. Previously, Lee et al. successfully separated them in graphene by examining correlations between the Raman G and 2D (G$'$) modes.[33] This approach has also been employed in several studies within the CNT field,[5,34] although they mainly focused on individual carbon nanotubes. Here, we use the (ω_{G^+}, ω_{2D}) correlation to further probe the pressure and doping effects in the SWCNT film system.

In Figure 4a, we present a summary of extensive measurements conducted on SWCNT and SWCNT@BNNT film samples with the aim of decoupling the pressure and doping effects. Overall, we have identified five distinct regions in the (ω_{G^+}, ω_{2D}) correlation plot. First, we define a region of pristine SWCNTs, represented by light purple downward-pointing triangles. These triangles represent different samples obtained from one batch of the SWCNT film deposited in one CVD process. Interestingly, the mean G and 2D-band frequencies in this region vary significantly from sample to sample, indicating the presence of large inhomogeneity in the films' properties, such as built-in strain or nonzero initial doping due to the ambient atmosphere.

Second, the growth of BN coating on the pristine SWCNT templates forms the second region with well-separated data clusters (blue circles with darker shading for longer growth time). Since both the G$^+$ and 2D band frequencies of inner SWCNTs gradually decrease, the data clusters align along a line with a slope $\Delta\omega_{2D}/\Delta\omega_G$) = 2.11 ± 0.02 (dashed line in Figure

4a; see also SI Section S6). This value closely matches the strain-induced curve with $\Delta\omega_{2D}/\Delta\omega_G$ = 2.2 ± 0.2, reported for graphene.[33]

Interestingly, upon thermal annealing, both the SWCNT-pristine and SWCNT@BNNT data clusters experience a G band upshift and 2D band downshift, establishing the third and fourth distinct regions represented by light green upper triangles and green squares, respectively. By fitting a line to all the points in the clouds, we obtain a slope $\Delta\omega_{2D}/\Delta\omega_G$ = 1.93 ± 0.02 (dotted dash line in Figure 4a), which is nearly within the error bar of the value reported for graphene.[33]

Finally, doping the annealed SWCNT samples by MoO$_3$ particles results in a simultaneous increase of the G and 2D band frequencies, forming the fifth region (purple diamonds). Again, by fitting all the points in the annealed and annealed-doped data clusters, we obtain a line with a slope $\Delta\omega_{2D}/\Delta\omega_G$ = 6.45 ± 0.15. We will discuss transitions between these different regions in the following sections.

However, we already want to highlight that the direction of the G$^+$ and 2D band frequency shifts due to different types of (de)doping in Figure 4a differs significantly from the shifts caused by the BN coating. Given that the latter effects align well with the direction of the strain effect in graphene, we can conclude that the downshifts of the G band and 2D band after the BNNT growth are primarily caused by the BNNT-induced pressure effect on SWCNTs, while the effect of doping due to BN deposition is minimal.

It is worth noting that the aforementioned effects can be observed when using various excitation wavelengths. For illustration, we selected pristine SWCNT and SWCNT@BNNT-60 film samples and performed Raman mapping measurements utilizing four different excitation lasers (488, 532, 633, and 785 nm), as detailed in SI Section S7. However, when analyzing the correlation between G$^+$ and 2D (G$'$) band frequencies, it is essential to consider that the latter exhibits an almost linear dependence on the laser energy, as was reported almost two decades ago.[35,36] Figure 4b illustrates this dependence for the pristine SWCNT film in our study. The least-squares fit for the measured dispersion of the 2D (G$'$) band is expressed by the equation

$$\omega_{2D}^{eq} = 2429 + 104.7 \cdot E_{laser} \tag{1}$$
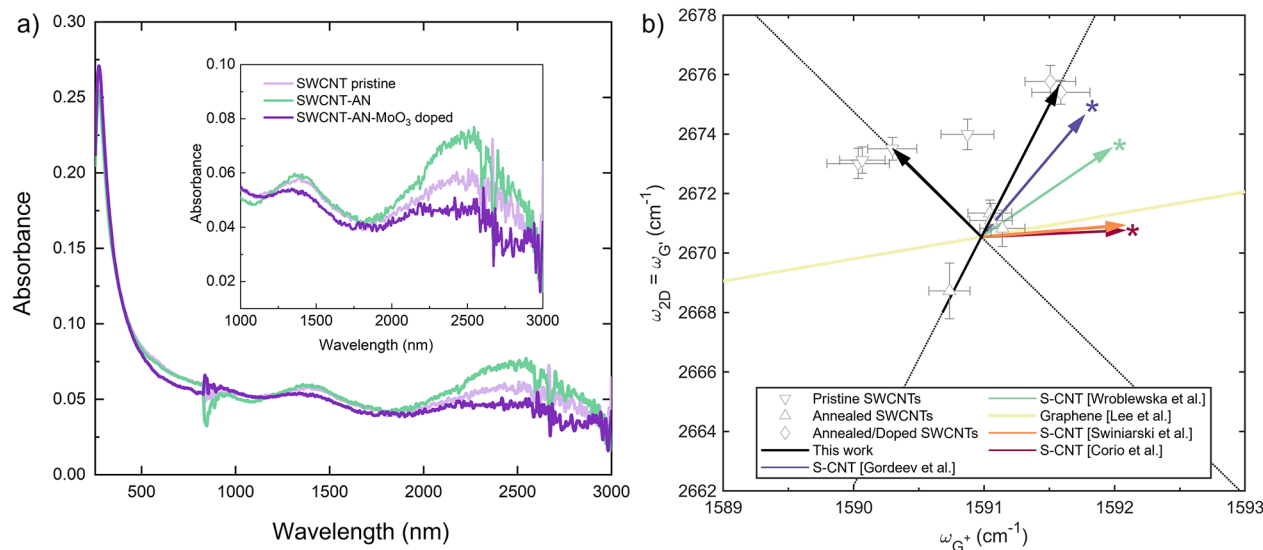
Figure 6. (a) Optical absorption spectra of the pristine SWCNT film, the annealed SWCNT film, and the MoO$_3$-doped annealed SWCNT film. The inset shows the zoomed-in absorption spectra with the range from 500 to 3000 nm of the same samples. (b) Correlation between the frequency of the G and 2D (G') Raman mode of the experimental data in this work and literature data. The literature data are from Gordeev et al.,[51] Wroblewska et al.,[52] Lee et al.,[33] Swiniarski et al.,[33] and Corio et al.[44] All vectors marked with an asterisk were scaled to fit the frequency range studied in this work.

where ω_{2D} and E_{laser} are measured in cm^{-1} and eV, respectively. The slope value we obtained in our SWCNT film (104.7 cm^{-1}/eV) is quite close to the value (106 cm^{-1}/eV) reported by Pimenta et al.[36] To consolidate data from multiple excitation measurements into a single plot, we subtracted the calculated frequency of the 2D band (ω_{2D}^{eq}) from the measured frequency (ω_{2D}^{exp}). In this way, we established the correlation between the frequencies of the G$^+$ peak and $\omega_{2D}^{exp} - \omega_{2D}^{eq}$ for both the SWCNT and SWCNT@BNNT film samples measured under four different excitation wavelengths (Figure 4c). We observed a clear downshift of the 2D (G') and G$^+$ frequencies upon BNNT growth, which closely follows the graphene strain curve[33] with the slope of 2.2 (green solid line).

Removal of the Initial Doping Effect on SWCNT Films.
The SWCNTs often exhibit p-type doping when exposed to air due to their interaction with the oxygen in the ambient atmosphere.[37,38] To remove this initial p-doping in our pristine SWCNT films, we employed a vacuum annealing method with various annealing temperatures and investigated the optimal conditions using UV−vis−NIR and Raman mapping. We found that the S$_{11}$ peak in absorption spectra of SWCNT films increases in intensity after the vacuum annealing treatment (Figure S14), confirming the removal of the doping induced by oxygen in the ambient atmosphere.[39,40]

We also observed the evolution of the G and 2D (G') band frequencies at different annealing temperatures, as depicted in Figure 5a. The 2D (G') band is recognized for its sensitivity to the doping effect,[41,42] with hole doping causing a blue shift and electron doping inducing a red shift in frequency.[43,44] For the G band, there is a consensus that hole doping leads to a frequency upshift.[45,46] In our case, after the vacuum annealing, the 2D (G') mode mean position of the SWCNT film shifted to lower frequencies, as expected for the dedoping of the pristine p-doped SWCNT film. Surprisingly, we also noted a slight upshift in the G band for the annealed SWCNT sample.

This unexpected G-band behavior aligns with a recent study by Grimm et al.,[47] which reported a small downshift of about 1

cm^{-1} at small to medium hole concentrations, followed by an upshift at high hole-doping values. This finding was particularly pronounced in mixed-chirality samples such as the films in this work. Therefore, the observed G band upshift can be attributed to the removal of the mild p-doping, as described by Grimm et al.[47] Furthermore, we cannot rule out the possibility that the G band upshift during vacuum annealing is not solely linked to doping but could also originate from strain relaxation at high temperatures.

Finally, direct evidence of the dedoping effect resulting from vacuum annealing is derived from the photoelectron yield spectroscopy (PYS) results (Figure S15), which reveal that the pristine SWCNT film possesses a deeper valence band (VB) energy level ($E_{VB} = -4.98$ eV) compared to the annealed SWCNT film ($E_{VB} = -4.9$ eV). Thus, this vacuum annealing method can significantly reduce the initial doping effect on the pristine SWCNT films. Since the dedoping effect is most pronounced at 550 °C (1 h), as evidenced by UV−vis−NIR and Raman data, and this temperature does not harm the SWCNT structure, we establish it as the standard for the following sections.

Air Decay of SWCNT Film and SWCNT@BNNT Heterostructure Film. To investigate how long it takes for SWCNT films to become doped again by the ambient atmosphere, we conducted UV−vis−NIR measurements on a freshly annealed SWCNT sample and monitored the evolution of doping through optical absorption spectra (Figure S16). We observed an increase in the intensity of the S$_{11}$ peak of the SWCNT film after the vacuum annealing process, which is consistent with previous findings. Then, after storing the sample in the air, we noticed a gradual decay in intensity, reaching levels lower than that of the pristine state 5 h after annealing. This observation suggests the active adsorption of oxygen onto the SWCNTs. However, the S$_{11}$ peak fully recovered to its original intensity after 20 days, possibly indicating the attainment of the final stable state in the oxygen adsorption process.

H

We also studied the air decay of the SWCNT and SWCNT@BNNT heterostructure films by monitoring the (ω_{G^+}, ω_{2D}) frequencies, as shown in Figure 5b. We found that these frequencies in the freshly annealed SWCNT sample (green squares) shifted back toward their original position in the pristine film after the sample was exposed to air for 101 days (orange squares). Similar behavior was observed in the SWCNT@BNNT heterostructure films after vacuum annealing and storing in the air for 85 days (Figure S17). These frequency changes can be explained by oxygen adsorption on the SWCNTs and align well with the UV−vis-NIR data.

Doping Effect on the SWCNT Film. Besides the mild doping induced by oxygen adsorption, we also investigated the stronger doping effects induced by MoO_3. MoO_3 has been previously reported as an effective dopant for CNT films due to its stability in various environments such as chemicals and humidity.[48,49] Here, we applied it to doping annealed SWCNT films through thermal deposition. In particular, we thermally evaporated MoO_3 layers of different nominal thickness (1 and 4 nm) onto the SWCNT films following the procedure from ref 50. We found that only a 4 nm MoO_3 layer forms a continuous coating on the SWCNT network, as is evident from the SEM images in Figure S18. Optical absorption spectra clearly reveal the dedoping effect after vacuum annealing and the doping effect after MoO_3 evaporation (4 nm case), as shown in Figure 6a.

We conducted a comparison between the shifts of the G^+ and 2D bands resulting from doping in our study and those reported in the literature for doped SWCNTs. This comparison involved calculating doping vectors that represent the direction of the frequency shifts (Figure 6b). To enhance clarity, we adjusted the origin of the literature doping vectors to align with the center of our experimental group "SWCNTs annealed" (represented by the light green triangles in Figure 4a). All vectors marked with an asterisk (*) were scaled to fit the frequency range studied in this work. We compiled literature data that reported p-type doping of semiconducting SWCNTs in Figure 6b to facilitate a direct comparison to our study. It is worth noting that the direction of the G^+ and 2D band shift resulting from oxygen adsorption differs significantly from that of the other vectors in the literature. However, the shift values observed in our study are smaller compared to the values reported in previous works. This discrepancy can be attributed to the more powerful doping methods employed in the literature, such as the electrochemical method[43,44] and covalent functionalization,[51] which can induce large shifts in the G^+ and 2D band frequencies. Overall, for p-doped semiconducting SWCNTs, the slope of the doping vectors varies, depending on the doping method. This diversity might arise from differences in doping levels or the strain induced during the doping process.

CONCLUSION

In conclusion, we thoroughly characterized the optical properties of SWCNT@BNNT heterostructure films by using UV−vis−NIR spectroscopy, FT-IR, and Raman spectroscopy. We investigated the pressure effect induced by BNNT wrapping on SWCNTs within the SWCNT@BNNT heterostructure film and demonstrated that the shifts in the G and 2D (G') modes of SWCNTs can serve as indicators of the efficiency of BNNT coating. Furthermore, we employed a vacuum annealing method to mitigate the initial doping effect on SWCNTs caused by exposure to an ambient atmosphere. This method effectively removes undesired doping and enhances the accuracy of

subsequent analyses. Moreover, the effect of MoO_3 doping of pristine SWCNT films was investigated by using UV−vis−NIR spectroscopy and Raman spectroscopy. We show that by conducting correlation analysis of the G and 2D (G') modes in Raman spectra, it is feasible to discern distinct types of doping effects as well as the influence of applied pressure on the SWCNTs within SWCNT@BNNT heterostructure films. This research contributes to a deeper understanding of the strain and doping effects in SWCNTs and SWCNT@BNNTs, which will be valuable for future studies of carbon nanotube-based 1D vdW heterostructures.

METHODS

Fabrication of SWCNT@BNNT Heterostructure Films. The pristine SWCNT film used in this work was synthesized by aerosol CVD.[26] Typically, ferrocene was used as the catalyst precursor and CO or ethanol was used as the carbon source. The SWCNTs were formed in the gas phase and collected on a filter. The SWCNTs then can be dry transferred onto a ceramic washer to build the SWCNT@BNNT heterostructure. After the preparation of the pristine SWCNT film, low-pressure CVD with 310 Pa was conducted to grow the SWCNT@BNNT heterostructure. Usually, the SWCNT film sample was placed at the center of the furnace. 38 mg of ammonia−borane complex (97%, Sigma-Aldrich) was loaded upstream and heated to 70 °C. The vapor of the BN precursor was carried by a flow of 200 sccm Ar (with 3% H_2) to the heating zone. The reaction temperature was 1250 °C, and the growth time varied from 15 to 60 min.

MoO_3 Doping and Vacuum Annealing of SWCNTs. SWCNT films were transferred onto glass substrates by a simple press-transfer method. Then, MoO_3 (Sigma-Aldrich) layers of different thicknesses (1 and 4 nm) were thermally evaporated onto the SWCNT films by a thermal evaporator from the ALS Technology Co., Ltd. For vacuum annealing treatment, samples in a tube furnace evacuated to 1 Pa were heated to a target temperature, then maintained at that temperature for 1 h, and after that cooled to room temperature.

SEM and TEM Characterizations. SEM images of the SWCNT film and SWCNT@BNNT heterostructure films were obtained by a Hitachi S-4800 instrument, operating at an accelerating voltage of 1 kV. TEM images were obtained with a JEM-2010F (acceleration voltage of 200 kV) and a JEM-ARM200F instrument (acceleration voltage of 80 kV).

Spectroscopic Characterizations. The UV−vis−NIR spectra were measured by a UV−vis-NIR spectrophotometer (UV-3150, Shimadzu). The FT-IR spectra were obtained by a Fourier-transform infrared spectrophotometer (IRPrestige-21, Shimadzu). The valence band measurement was performed using a photoemission yield spectrometer in air (Riken Keiki PYSA AC-3).

Raman spectra were acquired using a Renishaw inVia Raman spectrometer equipped with the following laser sources and diffraction gratings: 488 nm (2400 grooves/mm), 532 nm (1800 grooves/mm), 633 nm (1800 grooves/mm), and 785 nm (1200 grooves/mm). All measurements were performed in a backscattering geometry utilizing a 50× long-distance objective lens (NA = 0.5) under ambient conditions. To prevent potential heating effects on the SWCNTs, the laser power density used during measurements was varied in the range of 10−40 kW/cm². Raman mapping was performed in a point-by-point mode with a scanning area of 52 μm × 40 μm with 2 μm steps, including about 500−600 spectra for each sample. To address the calibration uncertainty during the long Raman mapping, we consistently measured reference silicon spectra immediately before and after conducting Raman mapping for each studied sample. We then adjusted the frequency of the Raman spectra in the map by half of the observed shift in the silicon peak (typical absolute shifts were on the order of only 0.25 cm^{-1}). Subsequently, each spectrum in the map was fitted by a set of Lorentzian line shapes and the information on the peak position, intensity, and fwhm was collected for subsequent statistical analysis (more details in SI Section S2).

ASSOCIATED CONTENT

ⓢ Supporting Information

The Supporting Information is available free of charge at https://pubs.acs.org/doi/10.1021/acsnano.3c09615.

SEM and TEM images of SWCNT@BNNT film for 30 and 60 min growth times, details of the processing and fitting of Raman maps of SWCNT and SWCNT@BNNT films, details of the fitting of frequency and fwhm distributions in individual and film samples of SWCNTs and SWCNT@BNNTs, effect of inhomogeneous broadening on the G-band of SWCNT@BNNT films, effect of hydrostatic pressure on the G-band of SWCNT@BNNT films, details of the fitting of strain and doping curves in 2D vs G frequency plots, wavelength-dependent resonant Raman spectroscopy of SWCNT and SWCNT@BNNT films, optical absorption spectra of vacuum annealing experiment and air decay behavior and PYS spectra of SWCNT film and SWCNT film after vacuum annealing treatment, Raman (ω_{G^+}, ω_{2D}) correlation map of air decay behavior from SWCNT@BNNT heterostructure films, and details of MoO_3 doping of SWCNT films (PDF)

AUTHOR INFORMATION

Corresponding Authors

Dmitry I. Levshov — *Department of Mechanical Engineering, The University of Tokyo, Tokyo 113-8656, Japan; Nanostructured and Organic Optical and Electronic Materials, Department of Physics, University of Antwerp, Antwerp 2610, Belgium;* ⓞ orcid.org/0000-0002-2249-7172; Email: dmitry.levshov@uantwerpen.be

Shigeo Maruyama — *Department of Mechanical Engineering, The University of Tokyo, Tokyo 113-8656, Japan;* ⓞ orcid.org/0000-0003-3694-3070; Email: maruyama@photon.t.u-tokyo.ac.jp

Authors

Shuhui Wang — *Department of Mechanical Engineering, The University of Tokyo, Tokyo 113-8656, Japan*

Keigo Otsuka — *Department of Mechanical Engineering, The University of Tokyo, Tokyo 113-8656, Japan;* ⓞ orcid.org/0000-0002-6694-0738

Bo-Wen Zhang — *Department of Mechanical Engineering, The University of Tokyo, Tokyo 113-8656, Japan*

Yongjia Zheng — *Department of Mechanical Engineering, The University of Tokyo, Tokyo 113-8656, Japan; State Key Laboratory of Fluid Power and Mechatronic Systems, School of Mechanical Engineering, Zhejiang University, Hangzhou 310027, People's Republic of China;* ⓞ orcid.org/0000-0001-5836-6978

Ya Feng — *Department of Mechanical Engineering, The University of Tokyo, Tokyo 113-8656, Japan;* ⓞ orcid.org/0000-0003-3049-9933

Ming Liu — *Department of Mechanical Engineering, The University of Tokyo, Tokyo 113-8656, Japan;* ⓞ orcid.org/0000-0002-5630-3874

Esko I. Kauppinen — *Department of Applied Physics, Aalto University School of Science, FI-00076 Aalto, Finland;* ⓞ orcid.org/0000-0003-1727-8810

Rong Xiang — *Department of Mechanical Engineering, The University of Tokyo, Tokyo 113-8656, Japan; State Key Laboratory of Fluid Power and Mechatronic Systems, School of*

Mechanical Engineering, Zhejiang University, Hangzhou 310027, People's Republic of China; ⓞ orcid.org/0000-0002-4775-4948

Shohei Chiashi — *Department of Mechanical Engineering, The University of Tokyo, Tokyo 113-8656, Japan;* ⓞ orcid.org/0000-0002-3813-0041

Wim Wenseleers — *Nanostructured and Organic Optical and Electronic Materials, Department of Physics, University of Antwerp, Antwerp 2610, Belgium*

Sofie Cambré — *Nanostructured and Organic Optical and Electronic Materials, Department of Physics, University of Antwerp, Antwerp 2610, Belgium;* ⓞ orcid.org/0000-0001-7471-7678

Complete contact information is available at:
https://pubs.acs.org/10.1021/acsnano.3c09615

Author Contributions

[⊥]S.W. and D.I.L. contributed equally to this work.

Notes

The authors declare no competing financial interest.

REFERENCES

(1) Xiang, R.; Inoue, T.; Zheng, Y.; Kumamoto, A.; Qian, Y.; Sato, Y.; Liu, M.; Tang, D.; Gokhale, D.; Guo, J.; Hisama, K.; Yotsumoto, S.; Ogamoto, T.; Arai, H.; Kobayashi, Y.; Zhang, H.; Hou, B.; Anisimov, A.; Maruyama, M.; Miyata, Y.; Okada, S.; Chiashi, S.; Li, Y.; Kong, J.; Kauppinen, E. I.; Ikuhara, Y.; Suenaga, K.; Maruyama, S. One-Dimensional van Der Waals Heterostructures. *Science* **2020**, *367* (6477), 537−542.

(2) Xiang, R.; Maruyama, S.; Li, Y. Building Blocks for One-Dimensional van Der Waals Heterostructures. *National Science Open* **2022**, *1* (3), 20220016.

(3) Xiang, R.; Maruyama, S.; Xiang, R.; Maruyama, S.; Sci, S. Heteronanotubes: Challenges and Opportunities. *Small Science* **2021**, *1* (2), 2000039.

(4) Feng, Y.; Li, H.; Inoue, T.; Chiashi, S.; Rotkin, S. V.; Xiang, R.; Maruyama, S. One-Dimensional van Der Waals Heterojunction Diode. *ACS Nano* **2021**, *15* (3), 5600−5609.

(5) Matsushita, S.; Otsuka, K.; Sugihara, T.; Zhu, G.; Kittipaisalsilpa, K.; Lee, M.; Xiang, R.; Chiashi, S.; Maruyama, S. Horizontal Arrays of One-Dimensional van Der Waals Heterostructures as Transistor Channels. *ACS Appl. Mater. Interfaces* **2023**, *15* (8), 10965−10973.

(6) Zhao, S.; Kitaura, R.; Moon, P.; Koshino, M.; Wang, F. Interlayer Interactions in 1D Van Der Waals Moiré Superlattices. *Advanced Science* **2022**, *9* (2), 2103460.

(7) Cambré, S.; Liu, M.; Levshov, D.; Otsuka, K.; Maruyama, S.; Xiang, R. Nanotube-Based 1D Heterostructures Coupled by van Der Waals Forces. *Small* **2021**, *17* (38), 2102585.

(8) Walker, K. E.; Rance, G. A.; Pekker, Á.; Tóháti, H. M.; Fay, M. W.; Lodge, R. W.; Stoppiello, C. T.; Kamarás, K.; Khlobystov, A. N. Growth of Carbon Nanotubes inside Boron Nitride Nanotubes by Coalescence

of Fullerenes: Toward the World's Smallest Coaxial Cable. *Small Methods* **2017**, *1* (9), 1700184.

(9) Hu, C.; Michaud-Rioux, V.; Yao, W.; Guo, H. Theoretical Design of Topological Heteronanotubes. *Nano Lett.* **2019**, *19* (6), 4146−4150.

(10) Liu, M.; Hisama, K.; Zheng, Y.; Maruyama, M.; Seo, S.; Anisimov, A.; Inoue, T.; Kauppinen, E. I.; Okada, S.; Chiashi, S.; Xiang, R.; Maruyama, S. Photoluminescence from Single-Walled MoS$_2$ Nanotubes Coaxially Grown on Boron Nitride Nanotubes. *ACS Nano* **2021**, *15* (5), 8418−8426.

(11) Burdanova, M. G.; Liu, M.; Staniforth, M.; Zheng, Y.; Xiang, R.; Chiashi, S.; Anisimov, A.; Kauppinen, E. I.; Maruyama, S.; Lloyd Hughes, J. Intertube Excitonic Coupling in Nanotube van Der Waals Heterostructures. *Adv. Funct Mater.* **2022**, *32* (11), 2104969.

(12) Zhang, R.; Feng, Y.; Li, H.; Kumamoto, A.; Wang, S.; Zheng, Y.; Dai, W.; Fang, N.; Liu, M.; Tanaka, T.; Kato, Y. K.; Kataura, H.; Ikuhara, Y.; Maruyama, S.; Xiang, R. Fabricating One-Dimensional van Der Waals Heterostructures on Chirality-Sorted Single-Walled Carbon Nanotubes. *Carbon* **2022**, *199*, 407−414.

(13) Zhang, C.; Fortner, J.; Wang, P.; Fagan, J. A.; Wang, S.; Liu, M.; Maruyama, S.; Wang, Y. Van Der Waals SWCNT@BN Heterostructures Synthesized from Solution-Processed Chirality-Pure Single-Wall Carbon Nanotubes. *ACS Nano* **2022**, *16*, 18630−18636.

(14) Michel, T.; Levshov, D.; Zahab, A.-A.; Sauvajol, J.-L.; Paillet, M. Probing the Intrinsic Vibrational and Optical Properties of Individual Chirality-Identified Carbon Nanotubes by Raman Spectroscopy. In *Handbook of Carbon Nanomaterials*; World Scientific: 2017; World Scientific Series on Carbon Nanoscience, Vols. 9 & 10, pp 75−112.

(15) Liu, K.; Hong, X.; Wu, M.; Xiao, F.; Wang, W.; Bai, X.; Ager, J. W.; Aloni, S.; Zettl, A.; Wang, E.; Wang, F. Quantum-Coupled Radial-Breathing Oscillations in Double-Walled Carbon Nanotubes. *Nature Communications* **2013**, *4* (1), 1375.

(16) Popov, V. N.; Levshov, D. I.; Sauvajol, J. L.; Paillet, M. Computational Study of the Shift of the G Band of Double-Walled Carbon Nanotubes Due to Interlayer Interactions. *Phys. Rev. B* **2018**, *97* (16), 165417.

(17) Levshov, D. I.; Tran, H. N.; Michel, T.; Cao, T. T.; Nguyen, V. C.; Arenal, R.; Popov, V. N.; Sauvajol, J. L.; Zahab, A. A.; Paillet, M. Interlayer Interaction Effects on the G Modes in Double-Walled Carbon Nanotubes With Different Electronic Configurations. *physica status solidi (b)* **2017**, *254* (11), 1700251.

(18) Levshov, D. I.; Avramenko, M. V.; Erkens, M.; Tran, H. N.; Cao, T. T.; Nguyen, V. C.; Flahaut, E.; Popov, V. N.; Zahab, A. A.; Sauvajol, J. L.; Arenal, R.; Wenseleers, W.; Cambré, S.; Paillet, M. Partial Quenching of Electronic Raman Scattering in Double-Wall Carbon Nanotubes by Interlayer Coupling. *Carbon* **2023**, *203*, 801−812.

(19) Erkens, M.; Levshov, D.; Wenseleers, W.; Li, H.; Flavel, B. S.; Fagan, J. A.; Popov, V. N.; Avramenko, M.; Forel, S.; Flahaut, E.; Cambré, S. Efficient Inner-to-Outer Wall Energy Transfer in Highly Pure Double-Wall Carbon Nanotubes Revealed by Detailed Spectroscopy. *ACS Nano* **2022**, *16* (10), 16038−16053.

(20) Gordeev, G.; Wasserroth, S.; Li, H.; Flavel, B.; Reich, S. Moiré-Induced Vibrational Coupling in Double-Walled Carbon Nanotubes. *Nano Lett.* **2021**, *21* (16), 6732−6739.

(21) Zhao, S.; Moon, P.; Miyauchi, Y.; Nishihara, T.; Matsuda, K.; Koshino, M.; Kitaura, R. Observation of Drastic Electronic-Structure Change in a One-Dimensional Moiré Superlattice. *Phys. Rev. Lett.* **2020**, *124* (10), 106101.

(22) Chalin, D. V.; Levshov, D. I.; Myasnikova, A. E.; Rochal, S. B. Tight-Binding Approximation for Bilayer Graphene and Nanotube Structures: From Commensurability to Incommensurability between the Layers. *Phys. Rev. B* **2022**, *105* (4), 045402.

(23) Paillet, M.; Popov, V. N.; Tran, H. N.; Blancon, J. C.; Levshov, D. I.; Arenal, R.; Parret, R.; Ayari, A.; San Miguel, A.; Vallée, F.; Del Fatti, N.; Zahab, A. A.; Sauvajol, J. L. Optically Active Cross-Band Transition in Double-Walled Carbon Nanotube and Its Impact on Raman Resonances. *Carbon* **2022**, *196*, 950−960.

(24) Liu, M.; Wang, S.; Zheng, Y.; Takeuchi, M.; Inoue, T.; Xiang, R.; Maruyama, S. Synthesis of Vertically Aligned Boron Nitride Nanotubes with a Template of Single-Walled Carbon Nanotubes. *J. Mater. Res.* **2022**, *37* (24), 4428−4437.

(25) Feng, Y.; Li, H.; Hou, B.; Kataura, H.; Inoue, T.; Chiashi, S.; Xiang, R.; Maruyama, S. Zeolite-Supported Synthesis, Solution Dispersion, and Optical Characterizations of Single-Walled Carbon Nanotubes Wrapped by Boron Nitride Nanotubes. *J. Appl. Phys.* **2021**, *129* (1), 015101.

(26) Nasibulin, A. G.; Kaskela, A.; Mustonen, K.; Anisimov, A. S.; Ruiz, V.; Kivistö, S.; Rackauskas, S.; Timmermans, M. Y.; Pudas, M.; Aitchison, B.; Kauppinen, M.; Brown, D. P.; Okhotnikov, O. G.; Kauppinen, E. I. Multifunctional Free-Standing Single-Walled Carbon Nanotube Films. *ACS Nano* **2011**, *5* (4), 3214−3221.

(27) Moisala, A.; Nasibulin, A. G.; Brown, D. P.; Jiang, H.; Khriachtchev, L.; Kauppinen, E. I. Single-Walled Carbon Nanotube Synthesis Using Ferrocene and Iron Pentacarbonyl in a Laminar Flow Reactor. *Chem. Eng. Sci.* **2006**, *61* (13), 4393−4402.

(28) Golberg, D.; Bando, Y.; Tang, C.; Zni, C. Boron Nitride Nanotubes. *Adv. Mater.* **2007**, *19* (18), 2413−2432.

(29) Lee, C. H.; Wang, J.; Kayatsha, V. K; Huang, J. Y; Yap, Y. K. Effective Growth of Boron Nitride Nanotubes by Thermal Chemical Vapor Deposition. *Nanotechnology* **2008**, *19* (45), 455605.

(30) Wirtz, L.; Rubio, A.; De La Concha, R.; Loiseau, A. Ab Initio Calculations of the Lattice Dynamics of Boron Nitride Nanotubes. *Phys. Rev. B* **2003**, *68* (4), 045425.

(31) Avramenko, M. V.; Hokkanen, M. J.; Slabodyan, Y.; Ahlskog, M.; Levshov, D. I. Role of Mechanical van Der Waals Coupling in the G -Band Splitting of Individual Multiwall Carbon Nanotubes. *J. Phys. Chem. C* **2022**, *126* (37), 15759−15767.

(32) Torres-Dias, A. C.; Cambré, S.; Wenseleers, W.; Machon, D.; San-Miguel, A. Chirality-Dependent Mechanical Response of Empty and Water-Filled Single-Wall Carbon Nanotubes at High Pressure. *Carbon* **2015**, *95*, 442−451.

(33) Lee, J. E.; Ahn, G.; Shim, J.; Lee, Y. S.; Ryu, S. Optical Separation of Mechanical Strain from Charge Doping in Graphene. *Nat. Commun.* **2012**, *3* (1), 1024.

(34) Yazda, K.; Tahir, S.; Michel, T.; Loubet, B.; Manghi, M.; Bentin, J.; Picaud, F.; Palmeri, J.; Henn, F.; Jourdain, V. Voltage-Activated Transport of Ions through Single-Walled Carbon Nanotubes. *Nanoscale* **2017**, *9* (33), 11976−11986.

(35) Kürti, J.; Zólyomi, V.; Grüneis, A.; Kuzmany, H. Double Resonant Raman Phenomena Enhanced by van Hove Singularities in Single-Wall Carbon Nanotubes. *Phys. Rev. B* **2002**, *65* (16), 165433.

(36) Pimenta, M. A.; Hanlon, E. B.; Marucci, A.; Corio, P.; Brown, S. D. M.; Empedocles, S. A.; Bawendi, M. G.; Dresselhaus, G.; Dresselhaus, M. S. The Anomalous Dispersion of the Disorder-Induced and the Second-Order Raman Bands in Carbon Nanotubes. *Brazilian Journal of Physics* **2000**, *30* (2), 423−427.

(37) Derycke, V.; Martel, R.; Appenzeller, J.; Avouris, P. Carbon Nanotube Inter- and Intramolecular Logic Gates. *Nano Lett.* **2001**, *1* (9), 453−456.

(38) Collins, P. G.; Bradley, K.; Ishigami, M.; Zettl, A. Extreme Oxygen Sensitivity of Electronic Properties of Carbon Nanotubes. *Science* **2000**, *287* (5459), 1801−1804.

(39) Tey, J. N.; Ho, X.; Wei, J. Effect of Doping on Single-Walled Carbon Nanotubes Network of Different Metallicity. *Nanoscale Res. Lett.* **2012**, *7*, 548.

(40) Zhang, B. W.; Lin, H. S.; Qiu, X. Y.; Shui, Q. J.; Zheng, Y. J.; Almesfer, M.; Kauppinen, E. I.; Matsuo, Y.; Maruyama, S. Spiro-OMeTAD versus PTAA for Single-Walled Carbon Nanotubes Electrode in Perovskite Solar Cells. *Carbon* **2023**, *205*, 321−327.

(41) Jorio, A.; Saito, R. Raman Spectroscopy for Carbon Nanotube Applications. *J. Appl. Phys.* **2021**, *129* (2), 021102.

(42) MacIel, I. O.; Anderson, N.; Pimenta, M. A.; Hartschuh, A.; Qian, H.; Terrones, M.; Terrones, H.; Campos-Delgado, J.; Rao, A. M.; Novotny, L.; Jorio, A. Electron and Phonon Renormalization near Charged Defects in Carbon Nanotubes. *Nature Materials* **2008**, *7* (11), 878−883.

(43) Hatting, B.; Heeg, S.; Ataka, K.; Heberle, J.; Hennrich, F.; Kappes, M. M.; Krupke, R.; Reich, S. Fermi Energy Shift in Deposited

Metallic Nanotubes: A Raman Scattering Study. *Phys. Rev. B* **2013**, *87* (16), 165442.

(44) Corio, P.; Santos, P. S.; Brar, V. W.; Samsonidze, G. G.; Chou, S. G.; Dresselhaus, M. S. Potential Dependent Surface Raman Spectroscopy of Single Wall Carbon Nanotube Films on Platinum Electrodes. *Chem. Phys. Lett.* **2003**, *370* (5−6), 675−682.

(45) Tsang, J. C.; Freitag, M.; Perebeinos, V.; Liu, J.; Avouris, P. Doping and Phonon Renormalization in Carbon Nanotubes. *Nat. Nanotechnol.* **2007**, *2* (11), 725−730.

(46) Das, A.; Sood, A. K.; Govindaraj, A.; Saitta, A. M.; Lazzeri, M.; Mauri, F.; Rao, C. N. R. Doping in Carbon Nanotubes Probed by Raman and Transport Measurements. *Phys. Rev. Lett.* **2007**, *99* (13), 136803.

(47) Grimm, S.; Schießl, S. P.; Zakharko, Y.; Rother, M.; Brohmann, M.; Zaumseil, J. Doping-Dependent G-Mode Shifts of Small Diameter Semiconducting Single-Walled Carbon Nanotubes. *Carbon* **2017**, *118*, 261−267.

(48) Jeon, I.; Cui, K.; Chiba, T.; Anisimov, A.; Nasibulin, A. G.; Kauppinen, E. I.; Maruyama, S.; Matsuo, Y. Direct and Dry Deposited Single-Walled Carbon Nanotube Films Doped with MoOx as Electron-Blocking Transparent Electrodes for Flexible Organic Solar Cells. *J. Am. Chem. Soc.* **2015**, *137* (25), 7982−7985.

(49) Hellstrom, S. L.; Vosgueritchian, M.; Stoltenberg, R. M.; Irfan, I.; Hammock, M.; Wang, Y. B.; Jia, C.; Guo, X.; Gao, Y.; Bao, Z. Strong and Stable Doping of Carbon Nanotubes and Graphene by MoO x for Transparent Electrodes. *Nano Lett.* **2012**, *12* (7), 3574−3580.

(50) Seo, S.; Akino, K.; Nam, J.-S.; Shawky, A.; Lin, H.-S.; Nagaya, H.; Kauppinen, E. I.; Xiang, R.; Matsuo, Y.; Jeon, I.; Maruyama, S. Multi-Functional MoO_3 Doping of Carbon-Nanotube Top Electrodes for Highly Transparent and Efficient Semi-Transparent Perovskite Solar Cells. *Adv. Mater. Interfaces* **2022**, *9* (1), 2101595.

(51) Gordeev, G.; Setaro, A.; Glaeske, M.; Jürgensen, S.; Reich, S. Doping in Covalently Functionalized Carbon Nanotubes: A Raman Scattering Study. *physica status solidi (b)* **2016**, *253* (12), 2461−2467.

(52) Wroblewska, A.; Gordeev, G.; Duzynska, A.; Reich, S.; Zdrojek, M. Doping and Plasmonic Raman Enhancement in Hybrid Single Walled Carbon Nanotubes Films with Embedded Gold Nanoparticles. *Carbon* **2021**, *179*, 531−540.

(53) Świniarski, M.; Dużyńska, A.; Gertych, A. P.; Czerniak-Łosiewicz, K.; Judek, J.; Zdrojek, M. Determination of the Electronic Transport in Type Separated Carbon Nanotubes Thin Films Doped with Gold Nanocrystals. *Sci. Rep.* **2021**, *11* (1), 16690.